ACSNANO

www.acsnano.org

ARTICLE

Portraits of Soot Molecules Reveal Pathways to Large Aromatics, Five-/Seven-Membered Rings, and Inception through π-Radical Localization

Leonard-Alexander Lieske,[#] Mario Commodo,[#] Jacob W. Martin, Katharina Kaiser, Vasiliki Benekou, Patrizia Minutolo, Andrea D'Anna,* and Leo Gross*

Cite This: *ACS Nano* 2023, 17, 13563−13574

Read Online

ACCESS | Metrics & More | Article Recommendations | Supporting Information

ABSTRACT: **Incipient soot early in the flame was studied by high-resolution atomic force microscopy and scanning tunneling microscopy to resolve the atomic structure and orbital densities of single soot molecules prepared on bilayer NaCl on Cu(111). We resolved extended catacondensed and pentagonal-ring linked (pentalinked) species indicating how small aromatics cross-link and cyclodehydrogenate to form moderately sized aromatics. In addition, we resolved embedded pentagonal and heptagonal rings in flame aromatics. These nonhexagonal rings suggest simultaneous growth through aromatic cross-linking/cyclodehydrogenation and hydrogen abstraction acetylene addition. Moreover, we observed three classes of open-shell π-radical species. First, radicals with an unpaired π-electron delocalized along the molecule's perimeter. Second, molecules with partially localized π-electrons at zigzag edges of a π-radical. Third, molecules with strong localization of a π-electron at pentagonal- and methylene-type sites. The third class consists of π-radicals localized enough to enable thermally stable bonds, as well as multiradical species such as diradicals in the open-shell triplet state. These π-diradicals can rapidly cluster through barrierless chain reactions enhanced by van der Waals interactions. These results improve our understanding of soot formation and the products formed by combustion and could provide insights for cleaner combustion and the production of hydrogen without CO_2 emissions.**

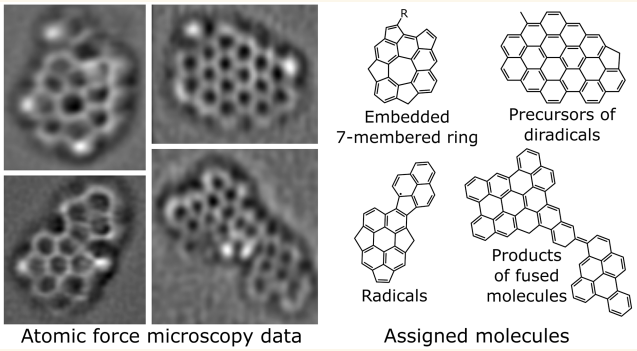

KEYWORDS: *Combustion, incipient soot, atomic force microscopy, scanning tunneling microscopy, single-molecule analysis*

INTRODUCTION

The mechanism by which soot particles, i.e., carbonaceous nanoparticles, are formed during the high-temperature incomplete combustion of hydrocarbon fuels is an object of ongoing research and is still being strongly debated in the combustion community. Particle inception, i.e., the transition from gas-phase polycyclic aromatic hydrocarbons (PAHs) to condensed-phase clusters or incipient soot,[1] remains the most intensely argued and yet most critical. Understanding the chemistry and physics behind this process is crucial in ultimately mitigating carbon particle emissions from combustion systems. The release of soot particles into the atmosphere is of great concern for human health and the environment, including climate heating.[2,3]

On the other side, understanding carbonaceous nanoparticle formation under combustion and pyrolytic conditions is motivated in the context of material science, such as producing carbon blacks,[4] or in the recent growing interest toward the environmentally friendly production of hydrogen via methane pyrolysis, namely "turquoise" hydrogen production, with low and possibly even negative carbon emissions.[5,6] Flame synthesis has emerged as an attractive technological method to produce other carbon nanostructures, including fullerenes, nanotubes, and graphene,[7] but also fluorescent carbon nanoparticles with tunable optical and electronic properties.[8]

Received: March 8, 2023
Accepted: July 5, 2023
Published: July 12, 2023

Downloaded via 150.241.217.2 on August 10, 2023 at 08:41:30 (UTC).
See https://pubs.acs.org/sharingguidelines for options on how to legitimately share published articles.

ACS Publications

© 2023 The Authors. Published by American Chemical Society

https://doi.org/10.1021/acsnano.3c02194
ACS Nano 2023, 17, 13563−13574

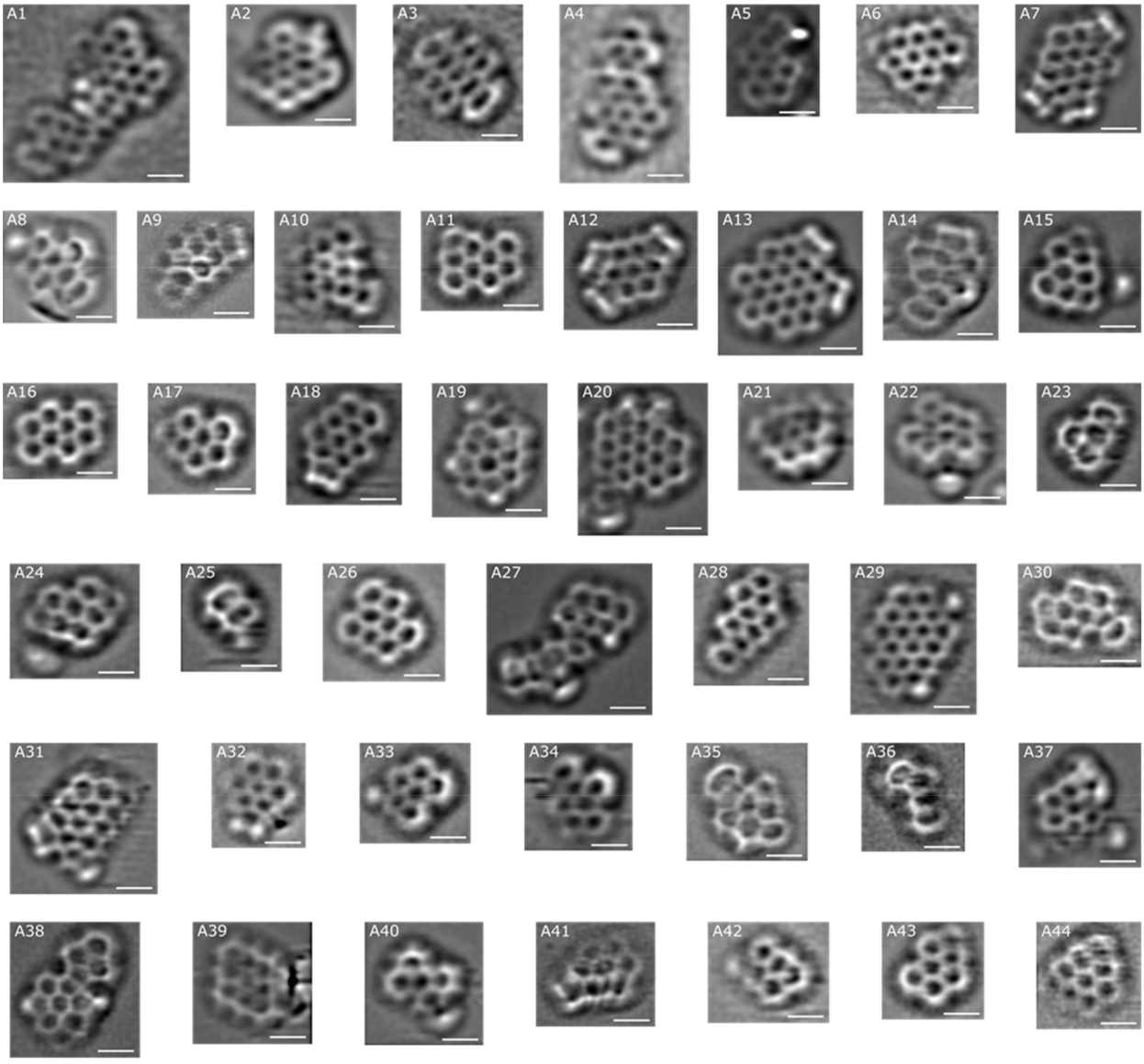

Figure 1. Laplace-filtered constant-height CO-tip AFM images of Z = 7 mm soot molecules. All molecules were measured on bilayer NaCl on Cu(111). Structures A1 to A31 are assigned with high confidence. Structures A32-A44 are tentatively assigned. All scale bars correspond to 5 Å. See Figures S1 to S6 for additional data.

In addition, PAHs and carbon nanoparticles, relevant to fuel-rich combustion, also attract considerable interest from the astrophysics community as analogues of carbonaceous molecules and grains in extraterrestrial environments.[9−11]

Given the above reasons, the formation of PAHs, condensed-phase carbonaceous species, and soot nanoparticles has been extensively investigated over the past decades and remains an ongoing and active research topic.[12−17] Particularly considering the formation mechanisms and the chemical characterization of incipient soot particles, significant progress has been made in the past few years both experimentally[18−23] and computationally.[24−30] Among the main advances, the identification of resonantly stabilized aromatic π-radicals (RSRs) as key intermediates in the nucleation and growth of soot particles has recently attracted major attention. Recent works have provided evidence for rapid molecular clustering-reaction pathways involving radical-chain reactions of RSRs, yet also suggesting the formation of covalently bound complexes.[18,28] In addition, the formation of fully or partially embedded five-membered ring structures may also contribute to the mass/molecular growth process.[31,32] The chemical growth of aromatic compounds is a pathway long sought in the soot community as an alternative or complementary route to the purely physical coalescence due to van der Waals/dispersion forces.[13,14] The relevance and implications of each of these two routes - physical and chemical pathways - alongside the combinations of both, have been thoroughly reviewed by Frenklach,[13] D'Anna,[14] and Wang[15] and, more recently, by Martin et al.[17,28]

Recently, atomic resolution noncontact atomic force microscopy with CO-functionalized tips (nc-AFM, hereafter abbreviated as AFM)[33] was used to study a variety of complex molecular mixtures based on atomically resolving single molecules including asphaltenes/heavy oil mixtures,[34,35] fuel pyrolysis products,[36] petroleum pitch,[37] molecules of meteoritic origin,[11] and aromatic molecules forming nascent soot nanoparticles.[19,20] The recent use of AFM,[19,20] for the analysis of the molecular constituents of the incipient soot particles, has

https://doi.org/10.1021/acsnano.3c02194
ACS Nano 2023, 17, 13563−13574

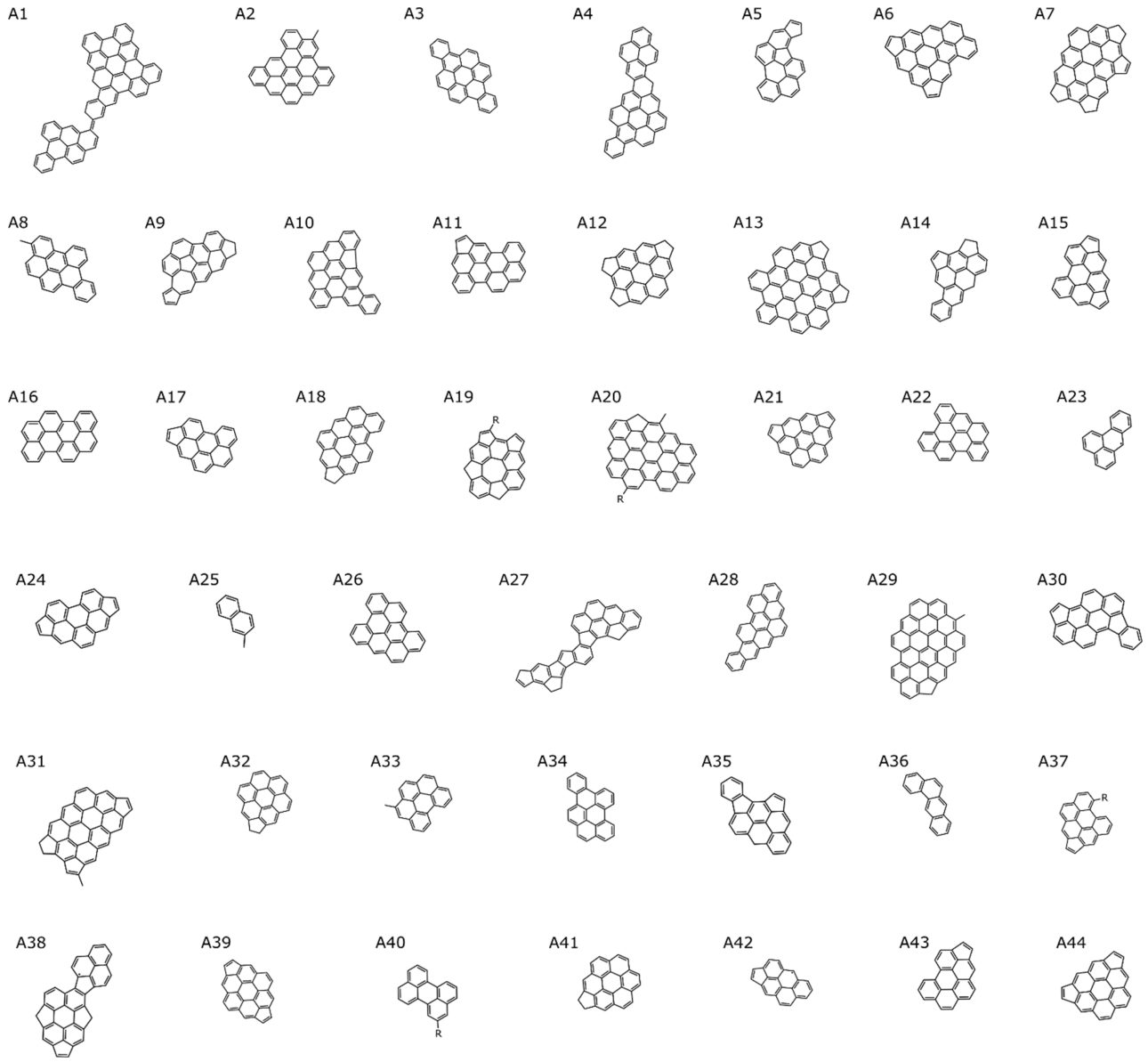

Figure 2. Assigned structures A1 to A31 and tentatively assigned structures A32 to A44 of the molecules for which AFM data are shown in Figure 1.

shed light on the richness in the molecular configurations and moieties of such compounds.

Here, for studying incipient soot, samples are collected from a lightly sooting laminar premixed flame of ethylene and air (see Methods). With increasing distance Z from the burner, the incipient soot particles grow and mature. Thus, collecting samples at different Z values can provide insight into the particle growth. The results obtained by these earlier applications of AFM studying soot at burner-to-probe separations of Z = 8 mm and Z = 14 mm have allowed, for instance, theoretically predicting a large variety of reactive sites of the observed molecules based on the different arrangement and hybridization of the carbon atoms at the edge of the molecules[24,25] as well as proposing possible routes for molecular growth and clustering.[26,27]

To achieve a better understanding of the chemical and physical processes involved during the high-temperature gas-to-particle transition, an in-depth knowledge of the molecular structure, properties, and conformations of the main chemical constituents and the precursors of the incipient particles is critical. Here, we investigate just-nucleated particles immediately behind the flame front of a fuel-rich ethylene-air flame, namely, at a probe-to-burner separation distance Z = 7 mm, thus accessing molecules in early soot formation, where particles are expected to be in the form of a molecular cluster rather than a nanocrystalline "solid" material. Due to their relatively small size and loosely bonded supramolecular structure, these incipient soot particles can provide aromatic molecules that can be studied by high-resolution atomic force microscopy providing insights into the inception process.

In this work, AFM measurements in combination with scanning tunneling microscopy (STM) orbital density imaging and atom manipulation are presented to elucidate the molecular structures of soot particles and discuss their implications for the growth process of incipient soot particles. Beneficial for the statistical significance of this study, most of the compounds of the Z = 7 mm condition could be resolved by AFM. Because recent investigations revealed the impor-

https://doi.org/10.1021/acsnano.3c02194
ACS Nano 2023, 17, 13563−13574

tance of open-shell π-radical systems in the soot formation process,[24−28] we refined our analysis by employing orbital density imaging with scanning tunneling microscopy (STM). To that end, we concentrated our investigation on the species found on bilayer NaCl islands. This insulating layer is used for electronic decoupling of the molecules from the metallic surface, preventing hybridization with the latter. This decoupling is beneficial for imaging the frontier orbital densities of the molecules by STM.[38] Electronic characterization by STM is important in two aspects: by comparison with calculated frontier orbital densities and spin densities, it corroborates and refines the structural assignments based on AFM.[34] Moreover, STM orbital images provide insight into the spin ground state and open-/closed-shell character of adsorbates.[28,39−43]

Atom manipulation was employed to mimic hydrogen dissociation processes taking place in the flame.[14−17,24−28] The atom manipulation experiments provide us with information about likely reaction pathways in flame, i.e., from which atomic sites hydrogen atoms are likely dissociated, and it also enables us to study the products formed by such dehydrogenations.

The most important findings of our study of molecules of the Z = 7 mm soot sample are 1) catacondensed and pentalinked molecules suggest cross-linking of small aromatics, 2) structures with partially and fully embedded five-membered and seven-membered rings suggest hydrogen abstraction acetylene addition (HACA) and cross-linking pathways occurring in tandem, and 3) different classes of open-shell π-radicals were found. Our analysis of the detected species reveals insights about the particle growth in the flame. These insights provide evidence for PAH growth and soot inception pathways and are of value to improving combustion processes and producing carbon materials alongside hydrogen production.

RESULTS AND DISCUSSION

Figure 1 shows AFM data of the molecules collected from the flame at a burner-to-probe separation distance of Z = 7 mm. They were evaporated from a Si-wafer onto a Cu(111) sample, partly covered with bilayer NaCl, at a sample temperature of about 10 K. Characterization has been performed by STM and AFM using a CO-functionalized tip at a sample temperature of T = 5 K, investigating individual molecules on bilayer NaCl on Cu(111). Most of the round bright features in the vicinity of molecules, e.g., near **A15** and **A24**, are CO molecules, which had been dosed on the surface for tip functionalization and are identified due to their dark contrast in constant-current STM images in conjunction with the AFM images (see Figures S1−S4).[33,44]

Figure 2 shows the assigned and tentatively assigned molecular structures. For the assignments, in addition to the AFM images shown in Figure 1, constant-height AFM images at different tip-heights have been obtained. Moreover, constant-current STM images at different sample voltages, corresponding to ion resonances, have been obtained and compared to DFT-calculated maps of the frontier orbital densities (Section 1 in the Supporting Information).

Compared to the Z = 8 mm sample earlier investigated by AFM,[19,20] for which about half of the molecules could not be analyzed at atomic resolution mostly because of some three-dimensional character, for the Z = 7 mm condition, the majority, i.e., about 80%, of the analyzed compounds could be resolved at the atomic scale (see STM overview in the Supporting Information, Figure S7), which is beneficial for the statistical significance of this study. This most likely is a result of the more planar morphology of the molecules. The Z = 7 mm sample contains mostly just-nucleated particles, whereas the Z = 8 mm sample presents more particles grown by coagulation;[45] for further details see the sample collection section in Methods. The Z = 8 mm sample can be expected to be more "graphitized" than the Z = 7 mm because particle carbonization/aging has been shown to be connected to particle coagulation.[46,47]

In the following paragraphs, we highlight specific features and discuss observations and implications of the molecules resolved in the Z = 7 mm sample. Figure 3 presents the H/C

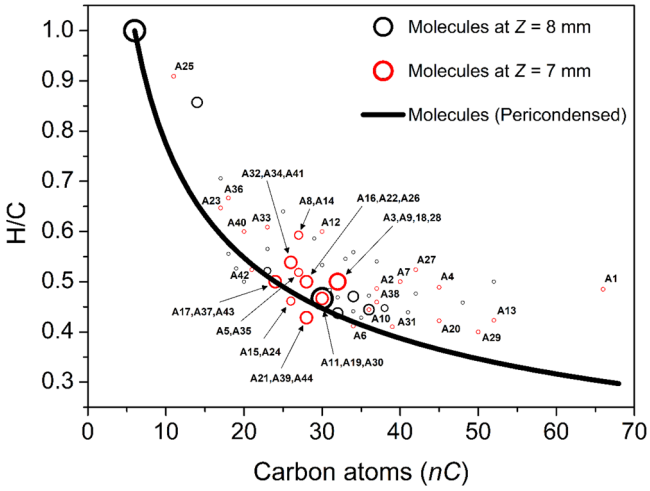

Figure 3. H/C ratio as a function of the number of aromatic carbon atoms (nC). Unknown side chains -R are counted as H. The line corresponds to the calculated trend for maximally pericondensed PAHs,[48] i.e., H/C = $(nC/6)^{-0.5}$; the black circles refer to molecules for the Z = 8 mm sample (from Commodo et al.[20]); red circles refer to the molecules of the Z = 7 mm sample (this work). Symbol sizes indicate the respective abundances in the sampled pool of molecules.

plots for molecules from the Z = 7 mm and the Z = 8 mm samples resolved by AFM. As for the Z = 8 mm condition, most of the aromatic molecules at Z = 7 mm are centered within the range of 20−40 carbon atoms (250−500 Da), with a typical H/C ratio of around 0.4−0.5 confirming earlier experimental and computational investigations that incipient soot is mainly composed by PAHs of moderate size and about the size of coronene to circumpyrene.[22,23,49]

The aromatic molecules are distributed close to the maximally pericondensed line (black line in Figure 3), but mainly in the H-rich region of the graph (top right). This is particularly evident as the mass of the molecules increases, and H/C almost reaches an asymptote for those exceeding 35 carbon atoms with a typical H/C ratio within the range of 0.4−0.5 (a pericondensed aromatic molecule with 50 C atoms has a H/C of 0.35). However, in a few cases, some molecules also lie below the maximally pericondensed line. This is, for instance, the case for **A21**, **A39**, and **A44**, which all present a compact aromatic structure with an extension on the periphery of some acenaphthylene groups. For the Z = 7 mm sample, a few very large (nC > 40) pericondensed structures, close to the maximally pericondensed line, are also detected. These are

https://doi.org/10.1021/acsnano.3c02194
ACS Nano 2023, 17, 13563−13574

molecules **A29** and **A20** reported in Figure 4a. These have 50 and 45 carbon atoms, respectively, with molecular masses of

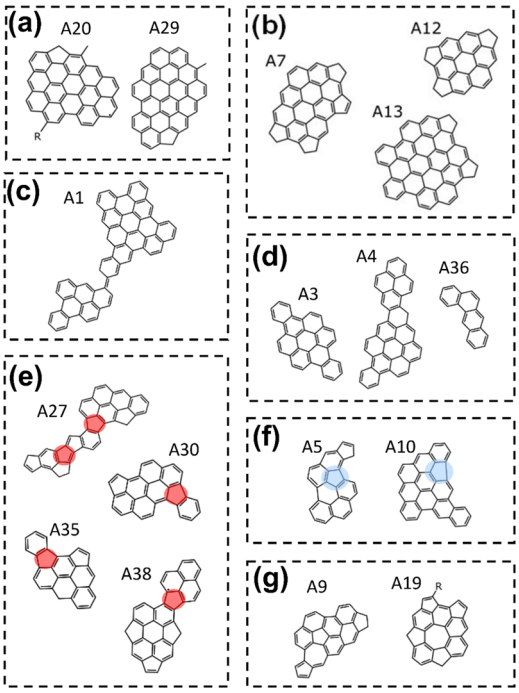

Figure 4. (a) Aromatic pericondensed structures with high molecular mass; (b) molecular species presenting substantial compact pericondensed structures but moving away from the maximally pericondensed line due to the aliphatic pentagonal rings at their periphery; (c) cross-linked aromatic molecule; (d) extended catacondensed and (e) pentalinked elongated structures; (f) aromatic molecules with partially embedded pentagonal rings. Highlights refer to molecules incorporating benzo[*ghi*]-fluoranthene-type moieties in which the five-membered ring is incorporated in one PAH core (blue); molecules incorporating fluoranthene-type moieties in which the five-membered ring is bridging two PAH cores (red); and (g) aromatic molecules incorporating both five- and seven-membered rings. Structure A9 presents a fully embedded five-membered ring, and structure A19 presents a fully embedded seven-membered ring.

621 and 560 Da (counting the unknown -R group in **A20** as -H). Both structures present a high degree of condensation, i.e., number of fused rings, with some aliphatic moieties, i.e., aliphatic substituted aromatics such as side chains (-R), methyl moieties, or methylene bridges in peripheral partially embedded pentagonal rings (fluorene-type configuration). This latter class of functionality is theoretically predicted to be formed from an "armchair" site (C4 motif) reacting with C1 gas-phase species.[50] The compound **A20** is also a resonance-stabilized PAH radical. The radical character of **A20** will be later discussed along with other detected open-shell species, such as dehydrogenated **A29**.

Another class of compounds of which several structures were detected features acenaphthene moieties, represented by compounds **A7**, **A12**, and **A13** that are reported in Figure 4b. Each of them, while presenting a high degree of pericondensation, has an H/C greater than the point on the maximally pericondensed line with the same number of carbon atoms. Notably, these structures present pentagonal rings on the edge of the molecule in the acenaphthene configuration. Acenaphthene, as well as acenaphthylene moieties, can be formed on a "zigzag"-type site of the molecule reacting with C2 gas-phase species, i.e., C_2H_4, C_2H_2.[50,51] Many (but not all, see structure **A7**) of the two peripheral C atoms of these pentagons are sp^3 hybridized, thus contributing to the relatively high degree of hydrogenation of the aromatic structures. **A13** possesses many bay edges that are unlikely to form via acetylene addition and could potentially indicate a ring-enlarging reaction of a rim-based pentagonal ring, recently shown between indenyl and methyl radicals.[52]

Evidence for cross-linking between aromatic species is found. Structure **A1** contains two PAH subunits cross-linked via a double bond (see Figure 4c). This motif was also observed in the cross-linked species **IS43**, detected in the $Z = 8$ mm sample.[20] Extended catacondensed species (Figure 4d) could form from HACA growth or cross-linking followed by cyclodehydrogenation (see Supporting Information section S4). The pentagonal ring-linked species shown in Figure 4e provide more conclusive evidence for cross-linking/cyclo-dehydrogenation between single aromatic units. The presence of single penta-links indicates cross-linking as seen in **A30** and **A35**, similar to that found for **IS30** in the $Z = 8$ mm sample.[20] Structure **A27** suggests the chemical dimerization between multiple aromatic moieties. **A27** also contains two adjacent pentagonal rings, a motif that has been hypothesized to occur by the formation of an E-bridge where cross-linking between an acenaphthylene-type edge and a zigzag edge leads to a bridge and dehydrogenation leads to two pentagonal rings connecting two PAH species.[16] However, **A27** is also likely to have formed from two fluorenyl-type edges cross-linking (see Supporting Information section S4). Such polymerization reactions followed by cyclodehydrogenation have long been suggested to explain the growth of small PAH to moderately sized aromatics. For example, Homann[31] found evidence in mass spectrometry for these species, which he called *aro*matic oligo*mers* (aromers). Cross-linked and cyclodehydrogenated PAH have long been computationally predicted.[53] Most recently, mass spectrometry experiments have found strong correlations between small and moderately sized soot PAH suggesting cross-links/dehydrogenation leading to loss of 2−6 hydrogens.[21]

Nonhexagonal rings were also observed either partially or fully embedded. Figure 4f shows aromatics that have partially embedded pentagonal rings. These can form from a large bay site that closes through cyclodehydrogenation to form a benzo[*ghi*]fluoranthene-type site.[54] But it could also form from a pentalink that is followed by acetylene addition to the bay site (see Supporting Information section S4).[55] In addition to the partially embedded five-membered rings, we also resolved a fully embedded five-membered ring and a fully embedded seven-membered ring; see **A9** and **A19** in Figure 4g, respectively. The **A9** compound has a central moiety made of a corannulene-like motif with the difference of presenting a seven-membered ring instead of a six-membered ring fused on one edge of the central five-membered ring. Due to the presence of the adjacent five-/seven-membered ring, such a molecule does not present significant curvature, evidenced by obtaining atomic resolution on the entire molecule with constant-height AFM, in contrast to, e.g., corannulene.[56,57] Molecule **A19** also presents a seven-membered ring fused to two five-membered rings. However, while in **A9** a five-membered ring is fully embedded, in **A19** the seven-membered ring is fully embedded. Like **A9**, **A19** also does not exhibit significant curvature because of the incorporation of fused five-

https://doi.org/10.1021/acsnano.3c02194
ACS Nano 2023, 17, 13563−13574

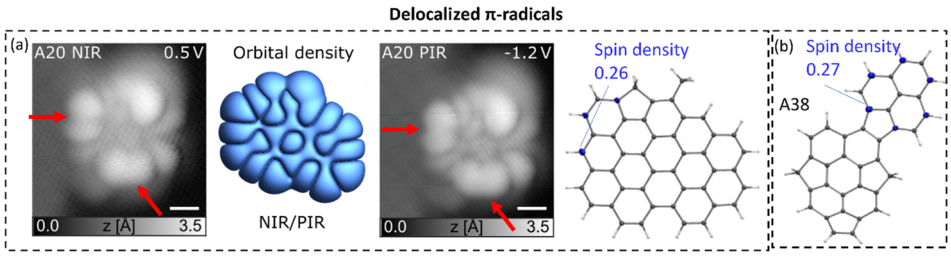

Figure 5. Delocalized π-radicals (a) A20 and (b) A38 structures with plots of their spin densities, i.e., Mulliken spin densities iso-surfaces of 0.025 au with the values of the carbon with the highest spin density indicated. (a) STM measurements of A20 at the first negative ion resonance (NIR, $V = 0.5$ V) and the first positive ion resonance (PIR, $V = -1.2$ V). The simulated orbital density corresponds to the density of the singly occupied molecular orbital, i.e., SOMO (which looks identical to the SUMO). Scale bars correspond to 5 Å. STM measurements were performed at a constant current of $I = 1$ pA.

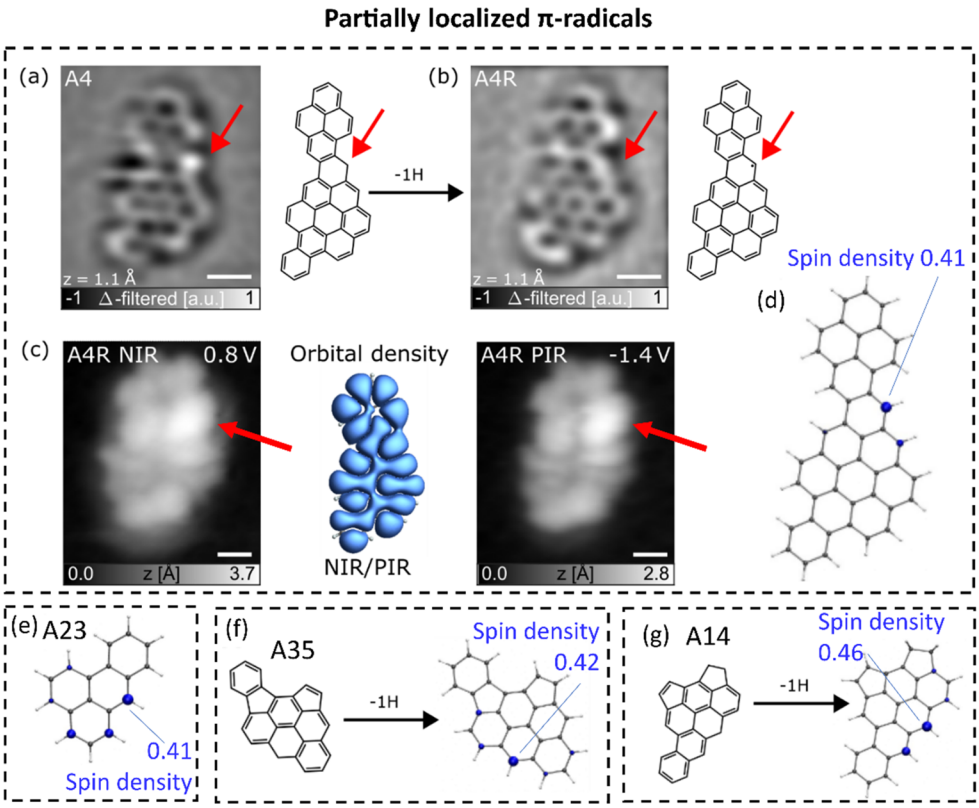

Figure 6. Partially localized π-radicals. Laplace-filtered AFM image and structure of (a) A4 and (b) A4R, generated by atom manipulation, with the position of the dissociated hydrogen indicated by red arrows. For dissociation, a voltage pulse $V = 4.5$ V was applied for 35 s with the tip positioned above the molecule. (c) STM measurements on A4R at the NIR, $V = 0.8$ V (left) and PIR, $V = -1.4$ V (right). Their very good agreement with the calculated SUMO/SOMO density (center) corroborates the assignment of A4 and A4R and the open-shell character of A4R. Scale bars correspond to 5 Å. STM measurements were performed at a constant current of $I = 1$ pA. Mulliken spin densities of the radicals (d) A4R, (e) A23, (f) dehydrogenated A35, and (g) dehydrogenated A14 are plotted in blue at iso-surfaces of 0.025 au with the highest spin population indicated.

and seven-membered ring moieties. The inclusion of pentagon-heptagon pairs is a characteristic motif of a dislocation defect, e.g., in Stone–Wales defects and grain boundaries, observed in carbon-based materials such as polycrystalline graphene, defective fullerenes, and carbon nanotubes.[58−62] Extended PAHs in the form of azulene-embedded nanographene structures have been synthesized as an important structural motif for tuning the chemical and electronic properties of PAHs.[63] However, the inclusion of heptagonal rings in flame-formed aromatics has rarely been observed in the combustion/soot community. Recently, Tian et al.[64] reported some experimental evidence on the formation of hydrogenated fullerene $C_{66}H_4$ with symmetric heptagonal rings from low-pressure flames. The possible inclusions of heptagon rings in the aromatic structures relevant to the soot formation process were theoretically proposed by Mao et al.[65] from reactive force field molecular dynamics simulations. More recently, Kraft and coauthors, in a series of theoretical contributions,[66,67] specifically focused on the formation and inclusion of five- and seven-membered rings in PAHs, showing how likely seven-membered rings could be formed under flame conditions. Using density functional theory calculations, the rates for the formation of seven-membered rings by HACA growth and bay closures (on a bay containing a five-membered ring) were shown to be similar to the analogous processes for the formation of five- and six-membered rings (see Supporting

https://doi.org/10.1021/acsnano.3c02194
ACS Nano 2023, 17, 13563−13574

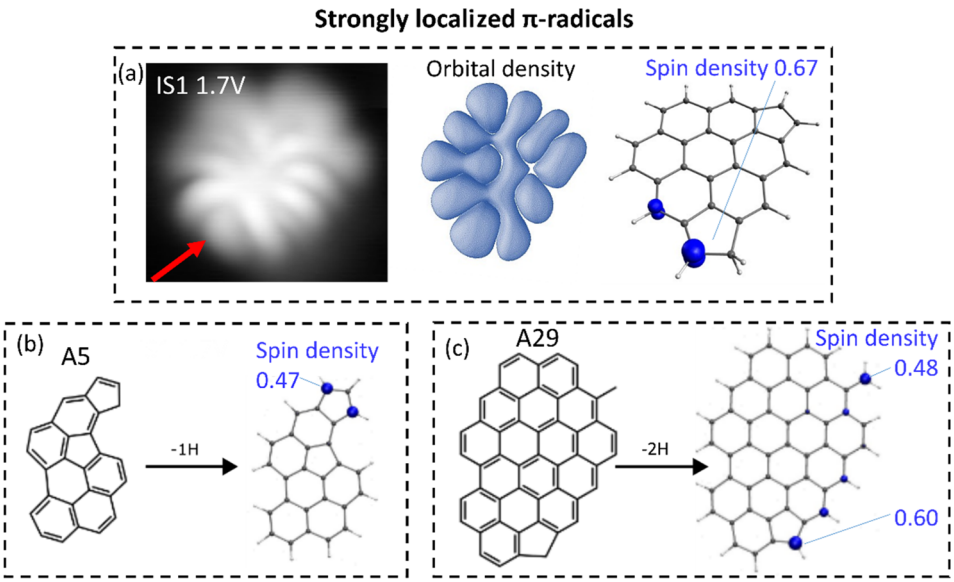

Figure 7. (a) STM measurements on IS1 at the NIR, V = 1.7 V, with the orbital density of the SOMO also plotted and the spin density shown as an iso = 0.025 au surface with maximal spin populations indicated. Dehydrogenated (b) A5 and (c) A29 were characterized with their corresponding spin densities and populations.

Information section S4).[66,67] However, many of these species suggest a cross-linking and cyclodehydrogenation reaction followed by HACA growth, as recently calculated for the E-bridge,[68] is the most likely path to form these extended structures with adjacent nonhexagonal rings.

The relevance of resonantly stabilized π-radicals, RSRs, in the generation, growth, and clustering of PAHs in high-temperature fuel-rich flames, has a central role in the discussion on the soot formation mechanism.[69−73] A mechanism involving aromatic π-radicals with localized π-electrons on zigzag edges was earlier suggested by Wang.[15] Recently, Johansson et al.[18] provided experimental evidence, by mass spectrometry measurements, for the presence of a pool of RSRs, including vinyl-cyclopentadienyl, thus proposing a mechanism based on radical-chain reactions propagation of RSRs that could promote aromatic growth. Further evidence on the "persistent radical character" of the pool of aromatics composing soot nanoparticles has also been recently obtained by molecular characterization by laser desorption laser ionization mass spectrometry measurements of soot extracted from both diffusion[22] and premixed laminar flames.[23] Recent measurements of nascent soot by electron paramagnetic resonance spectroscopy also indicated the presence of persistent radicals.[45,74] Schenk et al.[75] also provided evidence of the presence of RSRs in gas-phase samples extracted from several flames. Their analysis of the obtained mass spectra suggested that hydrogen removal from the saturated CH_2 group in PAHs containing five-membered rings, e.g., indene and fluorene, could result in the formation of very stable radical structures, i.e., RSRs, in concentrations comparable to those of the parent closed-shell structures. Our AFM results support this hypothesis. Several assigned aromatics present sp^3 carbons in methyl groups ($-CH_3$), which within the flame are expected to lose hydrogen and form methylene groups ($-CH_2$) and result in RSRs. However, different π-radicals present different reactivity, with only specific edge sites with localized π-radicals being able to form thermally stable cross-links.[24] Direct imaging of the bonding and electronic configurations within AFM and STM provides the opportunity to demonstrate the presence of these π-radicals and to analyze their π-electron localization.

Structures **A20** and **A38**, shown in Figure 5, are RSRs that possess delocalized π-electrons. A clear confirmation of its open-shell configuration has been measured for **A20** by STM orbital density imaging, shown in Figure 5a. Very similar images for the first negative ion resonance (NIR, V = 0.5 V) and the first positive ion resonance (PIR, V = −1.2 V) indicate the possibility of both adding and removing an electron to the same orbital, a hallmark of the open-shell character. The simulated orbital density shows the density of the singly unoccupied molecular orbital (SUMO), which is in excellent agreement with the measurements. The most pronounced maxima in the orbital density maps measured by STM are observed at the periphery of the molecule. The computed spin density is also found to be spread out along the perimeter of the aromatic. The maximum Mulliken spin population on a carbon atom is 0.26 indicating significant delocalization. It was computed that these delocalized π-radicals form bonds below 20 kcal/mol in strength.[24,26,76] The thermal stability of bonds within the flame is generally agreed to require bond strengths of more than 40 kcal/mol.[15] Thus, stronger localization of the π-electron is required for the formation of thermally stable bonds for inception. Nonetheless, these delocalized π-radicals do provide weak pancake and σ-bonds (∼20 kcal/mol) that could stabilize early incipient nanoparticles.[24,25]

The partial localization of the π-electron on zigzag edges is explored through atom manipulation experiments on **A4**, as shown in Figure 6a,b. Starting from the **A4** closed-shell molecule (Figure 6a) as found on the surface, the corresponding open-shell radical **A4R** (Figure 6b) was generated by tip-induced dehydrogenation with a voltage pulse V = 4.5 V applied above the molecule for 35 s. STM measurements on the formed **A4R** (Figure 6c) at the NIR, V = 0.8 V, and PIR, V = −1.4 V, and their very good agreement with the calculated SUMO/singly occupied molecular orbital (SOMO) density corroborate the assignment of **A4R** and its open-shell character and, in turn, also corroborate the assignment of **A4**. (Note that orbital densities of **A4** could

https://doi.org/10.1021/acsnano.3c02194
ACS Nano 2023, 17, 13563−13574

not be acquired by STM, because the molecule dislocated when the voltage was increased to map ionic resonances.) Calculated spin density isosurfaces of **A4R**, shown in Figure 6d, reveal the localization of the π-electron to the zigzag edge with a spin population of 0.41. The locations of high spin density coincide with the maximal protrusions measured by STM in the NIR and PIR images, as indicated by arrows in Figure 6c. This manipulation experiment, showing the dissociation of hydrogen from a CH_2 group, points toward this broken C−H bond being among the weakest bonds within the molecule and thus is in line with the hypothesis that such dissociation reactions occur in the flame.[24,26,75] However, our experiment is no proof of that process happening in the flame, because the situation in our tip-induced manipulation experiment at low temperature on a surface, where a molecular bond is broken by inelastic tunnelling of charge carriers[40,77−81] and also high electric fields between tip and sample might contribute to the reaction,[82,83] is very different from the situation in the flame.

The detected open-shell molecule **A23** shows a comparable π-electron localization as **A4R**, see Figure 6e. The hydrogenated zigzag edges of **A35** and **A14** shown in Figure 6f & 6g, respectively, present two more examples that could form partly localized open-shell species when dehydrogenated in the flame. The dehydrogenated **A14**, which features four aromatic rings involved in the zigzag edge, provides the strongest localization among these partially localized radicals. We have previously found that cross-linking between zigzag edges can reach bond energies of 30 kcal/mol.[24,26,76]

The strongest localization of π-electrons is found on pentagonal and methylene-type edges, with examples shown in Figure 7. Figure 7a shows the STM measurement of the NIR image and SOMO orbital density for the **IS1** species imaged in our previous paper.[28] The spin density shows strong localization to the edge, with a population of 0.67. For the structures **A5** and **A29**, strongly localized π-electrons can also be formed through dehydrogenation. The indenyl-type edge in **A5** leads to a localized π-electron spread between two sites, each with a spin population of 0.47. We have previously found these strongly localized π-radicals form bonds >40 kcal/mol in strength.[24,26,76]

These strongly localized π-radicals can also form diradicals. Dehydrogenation of **A29**, expected to occur under flame conditions, leads to the production of a localized π-diradical species with a triplet ground state.[28] Such species, comprising two localized radical sites, can rapidly form multiple cross-links through barrierless chain reactions enhanced by van der Waals interactions. The van der Waals interactions enable the lifetime of a physical dimer to be enhanced. By conformational changes and rotations of the molecules constituting a van der Waals bonded dimer, i.e., an internal rotor, the reactive sites have multiple opportunities to align and cross-link as recently discussed by Frenklach et al.[84] This mechanism of π-diradical inception to form soot is called polymerization of aromatic rim-linked hydrocarbons (PARLH).

CONCLUSIONS

We resolved individual molecules of incipient soot at the $Z = 7$ mm condition by high-resolution STM and AFM with CO-functionalized tips. We believe that, in the context of particle inception and growth, our results are important by providing specific structures of soot-formed molecules, including evidence for cross-linking, fully embedded five- and seven-membered rings, and providing an explanation for moderately sized aromatics formation. We report individual structures that feature open-shell π-radicals and analysis of the varying degrees of localization of the π-electrons. Delocalized π-radicals at the periphery of pericondensed aromatics provide weak localization and could provide some stabilizing multicenter bonds within the soot particles. Partially localized π-radicals on zigzag edges were found and generated by atom manipulation. Finally, we observed strongly localized π-radicals formed on pentagonal and methylene-type edges. These sites also provide opportunities for multiple reactive sites per molecule, such as in π-diradicals, that can react rapidly through the PARLH mechanism of inception. The flame aromatics detected in this work provide specific examples that allowed us to describe how molecules grow and cross-link in the flame, and they revealed the importance of π-radical localization. We hope that our findings can improve the fundamental understanding required for reducing soot formation in combustion, enhancing hydrogen production in pyrolysis, or explaining interstellar dust formation.

METHODS

Sample Collection. Incipient soot nanoparticles were collected from a lightly sooting laminar premixed flame of ethylene and air. The operating conditions were equivalent to those used in several earlier investigations,[23,85,86] including the previous AFM studies.[19,20] The flame has a cold gas velocity of 9.8 cm/s and equivalence ratio Φ = 2.01 and was stabilized on a water-cooled McKenna burner. Incipient soot, suspended in burned combustion gases, was extracted from the flame centerline using a high-dilution horizontal tubular probe positioned at a burner-to-probe separation distance $Z = 7$ mm, corresponding to the minimal distance that could be probed without perturbations of the flame front. The combustion products were sampled through a small orifice (200 μm in diameter), located on the bottom side of the dilution probe and rapidly mixed with N_2, providing a dilution ratio of 1:3000. A schematic view of the burner and soot sampling is reported in previous work.[20] The flame temperature was measured by an R-type thermocouple (Pt/Pt-13% Rh) with a spherical junction with a diameter of 300 μm with a rapid insertion procedure[87,88] and accounting for heat loss corrections.[89]

The size distribution of particles of this work was measured by a differential mobility analyzer (DMA): the aerosol sample passed through an X-ray charger (TSI model-3088) first and was then selected in an electrostatic classifier (DMA model-TapCon 3/150) and counted by a Faraday-cup electrometer.[86] The measured particle size distribution (PSD) is shown in Figure S9.

A stainless steel aerosol filter holder (Merck−Millipore model XX5004700) containing a quartz filter (Whatman QMA-grade, 47 mm) was positioned online downstream of the dilution tubular probe for soot collection. The gas temperature at the filter location was approximately 350 K. The sample collection lasted several hours to collect enough material on the filter for offline analysis.

On-Surface Sample Preparation for AFM Measurements. For sample preparation, a small Si wafer was covered with soot by softly pressing a soot-covered quartz filter on it. Afterward, the wafer was transferred into the ultrahigh vacuum (UHV) system, positioned in front of the cold sample ($T \approx 10$ K), and flash-annealed by Joule heating from room temperature to ∼900 K within a few seconds. This rapid heating can promote the process of sublimation over decomposition[90] and has been shown to work for molecules with masses up to ∼1000 Da.[91,92] An exemplary STM overview image is seen in Figure S7. About 80% of the compounds identified in an overview image as the one shown in Figure S7 could be resolved by atomic resolution AFM. For a detailed explanation of the preparation method and discussion of the representativeness of the assigned structures, see Supporting Information, sections S2 and S3.

https://doi.org/10.1021/acsnano.3c02194
ACS Nano 2023, 17, 13563−13574

STM and AFM Methods. The STM and AFM measurements were performed in a home-built combined STM/AFM setup[33,93] operating under ultrahigh vacuum (UHV) conditions ($p \approx 1 \times 10^{-10}$ mbar) and at low temperature ($T \approx 5$ K). The mode of operation is described in ref[33] and in more detail in ref,[94] and the different modes of operation and tip functionalization are reviewed in ref.[95] The microscope was equipped with a qPlus quartz sensor[96] operated in the frequency modulation mode.[97] As tip we used a PtIr-wire (25 μm in diameter) sharpened ex situ by focused ion beam milling and in situ by indentations into the bare Cu surface.

All STM images were measured in constant-current mode with a sample bias voltage V. AFM images were acquired in constant-height mode at $V = 0$ V. A Cu(111) single crystal was used as the substrate and partially covered with two monolayer (ML) thick NaCl(100) islands, denoted as NaCl(2 ML)/Cu(111). The tip was functionalized for AFM imaging by picking up a CO molecule from NaCl.[33,98] For AFM, this enabled high-resolution imaging. CO tip relaxations[99,100] lead to image distortions and can lead to apparent bonds but also enhance the contrast.[99,101] AFM is sensitive to the short-range Pauli repulsive force, resulting from the overlap of tip and sample wave functions.[102]

DFT Calculations. Density functional theory (DFT) calculations to calculate molecular geometries and frontier orbital densities were performed with Psi4 in the gas phase.[103] Geometry relaxations and subsequent single-point energy calculations utilized the B3LYP hybrid functional and the 6-31G basis set. The spin density calculations were performed in the ORCA 4.2.1 software.[104] The geometry optimizations were performed at the B3LYP/6-31G(d) level of theory with the spin density isosurface, and Mulliken atomic spin densities were calculated at the B3LYP/6-311G(d,p) level of theory. Multiwfn[105] was used to generate the cube files to visualize the spin density isosurfaces in Visual Molecular Dynamics.[106]

ASSOCIATED CONTENT

Supporting Information

The Supporting Information is available free of charge at https://pubs.acs.org/doi/10.1021/acsnano.3c02194.

Additional STM and AFM data and DFT results; statistical significance of the assigned molecules; details on sample collection; possible reaction pathways toward assigned structures; supplementary references (PDF)

AUTHOR INFORMATION

Corresponding Authors

Leo Gross − *IBM Research Europe − Zurich, 8803 Rüschlikon, Switzerland;* orcid.org/0000-0002-5337-4159; Email: lgr@zurich.ibm.com

Andrea D'Anna − *Dipartimento di Ingegneria Chimica, dei Materiali e della Produzione Industriale - Università degli Studi di Napoli Federico II, 80125 Napoli, Italy;* orcid.org/0000-0001-9018-3637; Email: anddanna@unina.it

Authors

Leonard-Alexander Lieske − *IBM Research Europe − Zurich, 8803 Rüschlikon, Switzerland*

Mario Commodo − *Istituto di Scienze e Tecnologie per l'Energia e la Mobilità Sostenibili, Consiglio Nazionale delle Ricerche, 80125 Napoli, Italy*

Jacob W. Martin − *Department of Physics and Astronomy, Curtin University, 6102 Perth, Australia;* orcid.org/0000-0002-7514-4549

Katharina Kaiser − *IBM Research Europe − Zurich, 8803 Rüschlikon, Switzerland;* Present Address: Present address: Université de Strasbourg, CNRS, IPCMS, UMR 7504, F-67000 Strasbourg, France; orcid.org/0000-0001-7519-8005

Vasiliki Benekou − *Institute of Organic Synthesis and Photoreactivity (ISOF), CNR Area della Ricerca di Bologna, 40129 Bologna, Italy*

Patrizia Minutolo − *Istituto di Scienze e Tecnologie per l'Energia e la Mobilità Sostenibili, Consiglio Nazionale delle Ricerche, 80125 Napoli, Italy*

Complete contact information is available at: https://pubs.acs.org/10.1021/acsnano.3c02194

Author Contributions

[#]L.-A.L. and M.C. contributed equally. L.-A.L., K.K., V.B., and L.G. performed the on-surface STM and AFM experiments. M.C., P.M., and A.D'A. performed the sample collection and DMA analysis. J.W.M. and L.-A.L. performed the DFT calculations. L.-A.L., L.G., M.C., A.D'A., and J.W.M. wrote the manuscript. All authors have given approval to the final version of the manuscript.

Funding

This work was financially supported by the H2020-MSCA-ITN ULTIMATE (grant number 813036), the European Union project SPRING (grant number 863098), and the European Research Council Synergy grant MolDAM (grant number 951519). J.W.M. would like to acknowledge funding from the Forrest Research Foundation Fellowship, the Australian Research Council through the Future Energy Export Cooperative Research Centre, and the Pawsey Supercomputer for computational resources. The work at University Federico II in Napoli was supported by the U.S. Air Force Office of Scientific Research (AFOSR) under grant number FA8655-21-1-7022.

Notes

The authors declare no competing financial interest.

REFERENCES

(1) Michelsen, H. A.; Colket, M. B.; Bengtsson, P.-E.; D'Anna, A.; Desgroux, P.; Haynes, B. S.; Miller, J. H.; Nathan, G. J.; Pitsch, H.; Wang, H. A Review of Terminology Used to Describe Soot Formation and Evolution under Combustion and Pyrolytic Conditions. *ACS Nano* **2020**, *14* (10), 12470−12490.

(2) Davidson, C. I.; Phalen, R. F.; Solomon, P. A. Airborne Particulate Matter and Human Health: A Review Airborne Particulate Matter and Human Health: A Review. *Aerosol Sci. Technol.* **2005**, *39*, 737−749.

(3) Bond, T. C.; Doherty, S. J.; Fahey, D. W.; Forster, P. M.; Berntsen, T.; Deangelo, B. J.; Flanner, M. G.; Ghan, S.; Kärcher, B.; Koch, D.; Kinne, S.; Kondo, Y.; Quinn, P. K.; Sarofim, M. C.; Schultz, M. G.; Schulz, M.; Venkataraman, C.; Zhang, H.; Zhang, S.; Bellouin, N.; Guttikunda, S. K.; Hopke, P. K.; Jacobson, M. Z.; Kaiser, J. W.; Klimont, Z.; Lohmann, U.; Schwarz, J. P.; Shindell, D.; Storelvmo, T.; Warren, S. G.; Zender, C. S. Bounding the Role of Black Carbon in the Climate System: A Scientific Assessment. *Journal of Geophysical Research Atmospheres* **2013**, *118* (11), 5380−5552.

(4) Kelesidis, G. A.; Goudeli, E.; Pratsinis, S. E. Flame Synthesis of Functional Nanostructured Materials and Devices: Surface Growth and Aggregation. *Proceedings of the Combustion Institute* **2017**, *36* (1), 29−50.

(5) Hermesmann, M.; Müller, T. E. Green, Turquoise, Blue, or Grey? Environmentally Friendly Hydrogen Production in Transforming Energy Systems. *Prog. Energy Combust. Sci.* **2022**, *90*, 100996.

(6) Diab, J.; Fulcheri, L.; Hessel, V.; Rohani, V.; Frenklach, M. Why Turquoise Hydrogen Will Be a Game Changer for the Energy Transition. *Int. J. Hydrogen Energy* **2022**, *47* (61), 25831−25848.

(7) Li, S.; Ren, Y.; Biswas, P.; Tse, S. D. Flame Aerosol Synthesis of Nanostructured Materials and Functional Devices: Processing, Modeling, and Diagnostics. *Prog. Energy Combust. Sci.* **2016**, *55*, 1−59.
(8) Liu, C.; Singh, A. V.; Saggese, C.; Tang, Q.; Chen, D.; Wan, K.; Vinciguerra, M.; Commodo, M.; de Falco, G.; Minutolo, P.; D'Anna, A.; Wang, H. Flame-Formed Carbon Nanoparticles Exhibit Quantum Dot Behaviors. *Proc. Natl. Acad. Sci. U. S. A.* **2019**, *116* (26), 12692.
(9) Allamandola, L. J.; Tielens, G. G. M.; Barker, J. R. Interstellar Polycyclic Aromatic Hydrocarbons - The Infrared Emission Bands, the Excitation/Emission Mechanism, and the Astrophysical Implications. *Astrophys J. Suppl Ser.* **1989**, *71*, 733.
(10) Kaiser, R. I.; Hansen, N. An Aromatic Universe-A Physical Chemistry Perspective. *J. Phys. Chem. A* **2021**, *125* (18), 3826−3840.
(11) Kaiser, K.; Schulz, F.; Maillard, J. F.; Hermann, F.; Pozo, I.; Peña, D.; Cleaves, H. J.; Burton, A. S.; Danger, G.; Afonso, C.; Sandford, S.; Gross, L. Visualization and Identification of Single Meteoritic Organic Molecules by Atomic Force Microscopy. *Meteorit Planet Sci.* **2022**, *57* (3), 644−656.
(12) Richter, H.; Howard, J. B. Formation of Polycyclic Aromatic Hydrocarbons and Their Growth to Soot-a Review of Chemical Reaction Pathways. *Prog. Energy Combust. Sci.* **2000**, *26* (4), 565−608.
(13) Frenklach, M. Reaction Mechanism of Soot Formation in Flames. *Phys. Chem. Chem. Phys.* **2002**, *4* (11), 2028−2037.
(14) D'Anna, A. Combustion-Formed Nanoparticles. *Proceedings of the Combustion Institute* **2009**, *32* (1), 593−613.
(15) Wang, H. Formation of Nascent Soot and Other Condensed-Phase Materials in Flames. *Proceedings of the Combustion Institute* **2011**, *33* (1), 41−67.
(16) Frenklach, M.; Mebel, A. M. On the Mechanism of Soot Nucleation. *Phys. Chem. Chem. Phys.* **2020**, *22* (9), 5314−5331.
(17) Martin, J. W.; Salamanca, M.; Kraft, M. Soot Inception: Carbonaceous Nanoparticle Formation in Flames: Soot Inception. *Prog. Energy Combust. Sci.* **2022**, *88*, 100956.
(18) Johansson, K. O.; Head-Gordon, M. P.; Schrader, P. E.; Wilson, K. R.; Michelsen, H. A. Resonance-Stabilized Hydrocarbon-Radical Chain Reactions May Explain Soot Inception and Growth. *Science* **2018**, *361* (6406), 997−1000.
(19) Schulz, F.; Commodo, M.; Kaiser, K.; De Falco, G.; Minutolo, P.; Meyer, G.; D'Anna, A.; Gross, L. Insights into Incipient Soot Formation by Atomic Force Microscopy. *Proceedings of the Combustion Institute* **2019**, *37* (1), 885−892.
(20) Commodo, M.; Kaiser, K.; De Falco, G.; Minutolo, P.; Schulz, F.; D'Anna, A.; Gross, L. On the Early Stages of Soot Formation: Molecular Structure Elucidation by High-Resolution Atomic Force Microscopy. *Combust. Flame* **2019**, *205*, 154.
(21) Faccinetto, A.; Irimiea, C.; Minutolo, P.; Commodo, M.; D'Anna, A.; Nuns, N.; Carpentier, Y.; Pirim, C.; Desgroux, P.; Focsa, C.; Mercier, X. Evidence on the Formation of Dimers of Polycyclic Aromatic Hydrocarbons in a Laminar Diffusion Flame. *Commun. Chem.* **2020**, *3* (1), 112.
(22) Jacobson, R. S.; Korte, A. R.; Vertes, A.; Miller, J. H. The Molecular Composition of Soot. *Angew. Chem., Int. Ed.* **2020**, *59* (11), 4484−4490.
(23) Sabbah, H.; Commodo, M.; Picca, F.; de Falco, G.; Minutolo, P.; D'Anna, A.; Joblin, C. Molecular Content of Nascent Soot: Family Characterization Using Two-Step Laser Desorption Laser Ionization Mass Spectrometry. *Proceedings of the Combustion Institute* **2021**, *38* (1), 1241−1248.
(24) Martin, J. W.; Hou, D.; Menon, A.; Pascazio, L.; Akroyd, J.; You, X.; Kraft, M. Reactivity of Polycyclic Aromatic Hydrocarbon Soot Precursors: Implications of Localized π-Radicals on Rim-Based Pentagonal Rings. *J. Phys. Chem. C* **2019**, *123* (43), 26673−26682.
(25) Gentile, F. S.; Picca, F.; de Falco, G.; Commodo, M.; Minutolo, P.; Causà, M.; D'Anna, A. Soot Inception: A DFT Study of σ and π Dimerization of Resonantly Stabilized Aromatic Radicals. *Fuel* **2020**, *279*, 118491.
(26) Menon, A.; Martin, J. W.; Leon, G.; Hou, D.; Pascazio, L.; You, X.; Kraft, M. Reactive Localized π-Radicals on Rim-Based Pentagonal Rings: Properties and Concentration in Flames. *Proceedings of the Combustion Institute* **2021**, *38* (1), 565−573.
(27) Pascazio, L.; Martin, J. W.; Menon, A.; Hou, D.; You, X.; Kraft, M. Aromatic Penta-Linked Hydrocarbons in Soot Nanoparticle Formation. *Proceedings of the Combustion Institute* **2021**, *38* (1), 1525−1532.
(28) Martin, J. W.; Pascazio, L.; Menon, A.; Akroyd, J.; Kaiser, K.; Schulz, F.; Commodo, M.; D'Anna, A.; Gross, L.; Kraft, M. π-Diradical Aromatic Soot Precursors in Flames. *J. Am. Chem. Soc.* **2021**, *143* (31), 12212−12219.
(29) Wang, Q.; Saldinger, J. C.; Elvati, P.; Violi, A. Molecular Structures in Flames: A Comparison between SNapS2 and Recent AFM Results. *Proceedings of the Combustion Institute* **2021**, *38* (1), 1133−1141.
(30) Nobili, A.; Pratali Maffei, L.; Baggioli, A.; Pelucchi, M.; Cuoci, A.; Cavallotti, C.; Faravelli, T. On the Radical Behavior of Large Polycyclic Aromatic Hydrocarbons in Soot Formation and Oxidation. *Combust. Flame* **2022**, *235*, 111692.
(31) Homann, K.-H. Fullerenes and Soot Formation— New Pathways to Large Particles in Flames. *Angew. Chem., Int. Ed.* **1998**, *37* (18), 2434−2451.
(32) Howard, J. B.; McKinnon, J. T.; Makarovsky, Y.; Lafleur, A. L.; Johnson, M. E. Fullerenes C60 and C70 in Flames. *Nature* **1991**, *352* (6331), 139−141.
(33) Gross, L.; Mohn, F.; Moll, N.; Liljeroth, P.; Meyer, G. The Chemical Structure of a Molecule Resolved by Atomic Force Microscopy. *Science* **2009**, *325* (5944), 1110−1114.
(34) Schuler, B.; Meyer, G.; Peña, D.; Mullins, O. C.; Gross, L. Unraveling the Molecular Structures of Asphaltenes by Atomic Force Microscopy. *J. Am. Chem. Soc.* **2015**, *137* (31), 9870−9876.
(35) Schuler, B.; Fatayer, S.; Meyer, G.; Rogel, E.; Moir, M.; Zhang, Y.; Harper, M. R.; Pomerantz, A. E.; Bake, K. D.; Witt, M.; Peña, D.; Kushnerick, J. D.; Mullins, O. C.; Ovalles, C.; van den Berg, F. G. A.; Gross, L. Heavy Oil Based Mixtures of Different Origins and Treatments Studied by Atomic Force Microscopy. *Energy Fuels* **2017**, *31* (7), 6856−6861.
(36) Fatayer, S.; Poddar, N. B.; Quiroga, S.; Schulz, F.; Schuler, B.; Kalpathy, S. v.; Meyer, G.; Pérez, D.; Guitián, E.; Peña, D.; Wornat, M. J.; Gross, L. Atomic Force Microscopy Identifying Fuel Pyrolysis Products and Directing the Synthesis of Analytical Standards. *J. Am. Chem. Soc.* **2018**, *140* (26), 8156−8161.
(37) Chen, P.; Metz, J. N.; Mennito, A. S.; Merchant, S.; Smith, S. E.; Siskin, M.; Rucker, S. P.; Dankworth, D. C.; Kushnerick, J. D.; Yao, N.; Zhang, Y. Petroleum Pitch: Exploring a 50-Year Structure Puzzle with Real-Space Molecular Imaging. *Carbon N Y* **2020**, *161*, 456−465.
(38) Repp, J.; Meyer, G.; Stojković, S. M.; Gourdon, A.; Joachim, C. Molecules on Insulating Films: Scanning-Tunneling Microscopy Imaging of Individual Molecular Orbitals. *Phys. Rev. Lett.* **2005**, *94* (2), 026803.
(39) Repp, J.; Meyer, G.; Paavilainen, S.; Olsson, F. E.; Persson, M. Imaging Bond Formation Between a Gold Atom and Pentacene on an Insulating Surface. *Science* **2006**, *312* (5777), 1196−1199.
(40) Pavliček, N.; Mistry, A.; Majzik, Z.; Moll, N.; Meyer, G.; Fox, D. J.; Gross, L. Synthesis and Characterization of Triangulene. *Nat. Nanotechnol* **2017**, *12* (4), 308−311.
(41) Majzik, Z.; Pavliček, N.; Vilas-Varela, M.; Pérez, D.; Moll, N.; Guitián, E.; Meyer, G.; Peña, D.; Gross, L. Studying an Antiaromatic Polycyclic Hydrocarbon Adsorbed on Different Surfaces. *Nat. Commun.* **2018**, *9* (1), 1198.
(42) Mishra, S.; Fatayer, S.; Fernández, S.; Kaiser, K.; Peña, D.; Gross, L. Nonbenzenoid High-Spin Polycyclic Hydrocarbons Generated by Atom Manipulation. *ACS Nano* **2022**, *16* (2), 3264−3271.
(43) Li, C.; Liu, Y.; Liu, Y.; Xue, F.-H.; Guan, D.; Li, Y.; Zheng, H.; Liu, C.; Jia, J.; Liu, P.-N.; Li, D.-Y.; Wang, S. Topological Defects Induced High-Spin Quartet State in Truxene-Based Molecular Graphenoids. *CCS Chemistry* **2023**, *5*, 695−703.

https://doi.org/10.1021/acsnano.3c02194
ACS Nano 2023, 17, 13563−13574

(44) Kaiser, K.; Scriven, L. M.; Schulz, F.; Gawel, P.; Gross, L.; Anderson, H. L. An Sp-Hybridized Molecular Carbon Allotrope, Cyclo[18]Carbon. *Science* **2019**, *365* (6459), 1299−1301.
(45) Vitiello, G.; de Falco, G.; Picca, F.; Commodo, M.; D'Errico, G.; Minutolo, P.; D'Anna, A. Role of Radicals in Carbon Clustering and Soot Inception: A Combined EPR and Raman Spectroscopic Study. *Combust. Flame* **2019**, *205*, 286−294.
(46) Basile, G.; Rolando, A.; D'Alessio, A.; D'Anna, A.; Minutolo, P. Coagulation and Carbonization Processes in Slightly Sooting Premixed Flames. *Proceedings of the Combustion Institute* **2002**, *29* (2), 2391−2397.
(47) Martin, J. W.; Botero, M.; Slavchov, R. I.; Bowal, K.; Akroyd, J.; Mosbach, S.; Kraft, M. Flexoelectricity and the Formation of Carbon Nanoparticles in Flames. *J. Phys. Chem. C* **2018**, *122* (38), 22210−22215.
(48) Solum, M. S.; Pugmire, R. J.; Grant, D. M. Carbon-13 Solid-State NMR of Argonne-Premium Coals. *Energy Fuels* **1989**, *3* (2), 187−193.
(49) Adkins, E. M.; Miller, J. H. Extinction Measurements for Optical Band Gap Determination of Soot in a Series of Nitrogen-Diluted Ethylene/Air Non-Premixed Flames. *Phys. Chem. Chem. Phys.* **2015**, *17* (4), 2686−2695.
(50) Shi, X.; Wang, Q.; Violi, A. Reaction Pathways for the Formation of Five-Membered Rings onto Polyaromatic Hydrocarbon Framework. *Fuel* **2021**, *283*, 119023.
(51) Whitesides, R.; Frenklach, M. Detailed Kinetic Monte Carlo Simulations of Graphene-Edge Growth. *J. Phys. Chem. A* **2010**, *114* (2), 689−703.
(52) Zhao, L.; Kaiser, R. I.; Lu, W.; Xu, B.; Ahmed, M.; Morozov, A. N.; Mebel, A. M.; Howlader, A. H.; Wnuk, S. F. Molecular Mass Growth through Ring Expansion in Polycyclic Aromatic Hydrocarbons via Radical-Radical Reactions. *Nat. Commun.* **2019**, *10* (1), 3689.
(53) Violi, A.; D'Anna, A.; D'Alessio, A. A Modeling Evaluation of the Effect of Chlorine on the Formation of Particulate Matter in Combustion. *Chemosphere* **2001**, *42* (5−7), 463−471.
(54) Frenklach, M.; Ebert, L. B. Comment on the Proposed Role of Spheroidal Carbon Clusters in Soot Formation. *J. Phys. Chem.* **1988**, *92* (2), 561−563.
(55) Tuli, L. B.; Mebel, A. M.; Frenklach, M. Bay Capping via Acetylene Addition to Polycyclic Aromatic Hydrocarbons: Mechanism and Kinetics. *Proceedings of the Combustion Institute* **2023**, *39*, 969.
(56) Wäckerlin, C.; Gallardo, A.; Mairena, A.; Baljozović, M.; Cahlík, A.; Antalík, A.; Brabec, J.; Veis, L.; Nachtigallová, D.; Jelínek, P.; Ernst, K.-H. On-Surface Hydrogenation of Buckybowls: From Curved Aromatic Molecules to Planar Non-Kekulé Aromatic Hydrocarbons. *ACS Nano* **2020**, *14* (12), 16735−16742.
(57) Martin, J. W.; Bowal, K.; Menon, A.; Slavchov, R. I.; Akroyd, J.; Mosbach, S.; Kraft, M. Polar Curved Polycyclic Aromatic Hydrocarbons in Soot Formation. *Proceedings of the Combustion Institute* **2019**, *37* (1), 1117−1123.
(58) Stone, A. J.; Wales, D. J. Theoretical Studies of Icosahedral C60 and Some Related Species. *Chem. Phys. Lett.* **1986**, *128* (5−6), 501−503.
(59) Yazyev, O. v.; Louie, S. G. Topological Defects in Graphene: Dislocations and Grain Boundaries. *Phys. Rev. B* **2010**, *81* (19), 195420.
(60) Huang, P. Y.; Ruiz-Vargas, C. S.; van der Zande, A. M.; Whitney, W. S.; Levendorf, M. P.; Kevek, J. W.; Garg, S.; Alden, J. S.; Hustedt, C. J.; Zhu, Y.; Park, J.; McEuen, P. L.; Muller, D. A. Grains and Grain Boundaries in Single-Layer Graphene Atomic Patchwork Quilts. *Nature* **2011**, *469* (7330), 389−392.
(61) Srinivasan, S. G.; van Duin, A. C. T.; Ganesh, P. Development of a ReaxFF Potential for Carbon Condensed Phases and Its Application to the Thermal Fragmentation of a Large Fullerene. *J. Phys. Chem. A* **2015**, *119* (4), 571−580.
(62) Klein, B. P.; Ihle, A.; Kachel, S. R.; Ruppenthal, L.; Hall, S. J.; Sattler, L.; Weber, S. M.; Herritsch, J.; Jaegermann, A.; Ebeling, D.; Maurer, R. J.; Hilt, G.; Tonner-Zech, R.; Schirmeisen, A.; Gottfried, J. M. Topological Stone-Wales Defects Enhance Bonding and Electronic Coupling at the Graphene/Metal Interface. *ACS Nano* **2022**, *16* (8), 11979−11987.
(63) Liu, J.; Mishra, S.; Pignedoli, C. A.; Passerone, D.; Urgel, J. I.; Fabrizio, A.; Lohr, T. G.; Ma, J.; Komber, H.; Baumgarten, M.; Corminboeuf, C.; Berger, R.; Ruffieux, P.; Müllen, K.; Fasel, R.; Feng, X. Open-Shell Nonbenzenoid Nanographenes Containing Two Pairs of Pentagonal and Heptagonal Rings. *J. Am. Chem. Soc.* **2019**, *141* (30), 12011−12020.
(64) Tian, H.-R.; Chen, M.-M.; Wang, K.; Chen, Z.-C.; Fu, C.-Y.; Zhang, Q.; Li, S.-H.; Deng, S.-L.; Yao, Y.-R.; Xie, S.-Y.; Huang, R.-B.; Zheng, L.-S. An Unconventional Hydrofullerene $C_{66}H_4$ with Symmetric Heptagons Retrieved in Low-Pressure Combustion. *J. Am. Chem. Soc.* **2019**, *141* (16), 6651−6657.
(65) Mao, Q.; van Duin, A. C. T.; Luo, K. H. Formation of Incipient Soot Particles from Polycyclic Aromatic Hydrocarbons: A ReaxFF Molecular Dynamics Study. *Carbon N Y* **2017**, *121*, 380−388.
(66) Menon, A.; Leon, G.; Akroyd, J.; Kraft, M. A Density Functional Theory Study on the Kinetics of Seven-Member Ring Formation in Polyaromatic Hydrocarbons. *Combust. Flame* **2020**, *217*, 152−174.
(67) Leon, G.; Menon, A.; Pascazio, L.; Bringley, E. J.; Akroyd, J.; Kraft, M. Kinetic Monte Carlo Statistics of Curvature Integration by HACA Growth and Bay Closure Reactions for PAH Growth in a Counterflow Diffusion Flame. *Proceedings of the Combustion Institute* **2021**, *38* (1), 1449−1457.
(68) Frenklach, M.; Mebel, A. M. On the Mechanism of Soot Nucleation. IV. Molecular Growth of the Flattened E-Bridge. *J. Phys. Chem. A* **2022**, *126* (49), 9259−9267.
(69) Howard, J. B. Carbon Addition and Oxidation Reactions in Heterogeneous Combustion and Soot Formation. *Symposium (International) on Combustion* **1991**, *23* (1), 1107−1127.
(70) Wagner, H. GG. Soot Formation in Combustion. *Symposium (International) on Combustion* **1979**, *17* (1), 3−19.
(71) Homann, K. H.; Wagner, H. Gg. Some New Aspects of the Mechanism of Carbon Formation in Premixed Flames. *Symposium (International) on Combustion* **1967**, *11* (1), 371−379.
(72) Keller, A.; Kovacs, R.; Homann, K.-H. Large Molecules, Ions, Radicals and Small Soot Particles in Fuel-Rich Hydrocarbon Flames. Part IV. Large Polycyclic Aromatic Hydrocarbons and Their Radicals in a Fuel-Rich Benzene-Oxygen Flame. *Phys. Chem. Chem. Phys.* **2000**, *2* (8), 1667−1675.
(73) D'Anna, A.; Violi, A.; D'Alessio, A.; Sarofim, A. F. A Reaction Pathway for Nanoparticle Formation in Rich Premixed Flames. *Combust. Flame* **2001**, *127* (1−2), 1995−2003.
(74) Commodo, M.; Picca, F.; Vitiello, G.; de Falco, G.; Minutolo, P.; D'Anna, A. Radicals in Nascent Soot from Laminar Premixed Ethylene and Ehtylene-Benzene Flames by Electron Paramagnetic Resonance Spectroscopy. *Proceedings of the Combustion Institute* **2021**, *38*, 1487.
(75) Schenk, M.; Hansen, N.; Vieker, H.; Beyer, A.; Gölzhäuser, A.; Kohse-Höinghaus, K. PAH Formation and Soot Morphology in Flames of C4 Fuels. *Proceedings of the Combustion Institute* **2015**, *35* (2), 1761−1769.
(76) Menon, A.; Martin, J. W.; Akroyd, J.; Kraft, M. Reactivity of Polycyclic Aromatic Hydrocarbon Soot Precursors: Kinetics and Equilibria. *J. Phys. Chem. A* **2020**, *124* (48), 10040−10052.
(77) Ladenthin, J. N.; Grill, L.; Gawinkowski, S.; Liu, S.; Waluk, J.; Kumagai, T. Hot Carrier-Induced Tautomerization within a Single Porphycene Molecule on Cu(111). *ACS Nano* **2015**, *9* (7), 7287−7295.
(78) Schendel, V.; Borca, B.; Pentegov, I.; Michnowicz, T.; Kraft, U.; Klauk, H.; Wahl, P.; Schlickum, U.; Kern, K. Remotely Controlled Isomer Selective Molecular Switching. *Nano Lett.* **2016**, *16* (1), 93−97.
(79) Pavliček, N.; Majzik, Z.; Collazos, S.; Meyer, G.; Pérez, D.; Guitián, E.; Peña, D.; Gross, L. Generation and Characterization of a

https://doi.org/10.1021/acsnano.3c02194
ACS Nano 2023, 17, 13563−13574

Meta -Aryne on Cu and NaCl Surfaces. *ACS Nano* **2017**, *11* (11), 10768−10773.
(80) Kim, Y.; Komeda, T.; Kawai, M. Single-Molecule Reaction and Characterization by Vibrational Excitation. *Phys. Rev. Lett.* **2002**, *89* (12), 126104.
(81) Hla, S.-W.; Bartels, L.; Meyer, G.; Rieder, K.-H. Inducing All Steps of a Chemical Reaction with the Scanning Tunneling Microscope Tip: Towards Single Molecule Engineering. *Phys. Rev. Lett.* **2000**, *85* (13), 2777−2780.
(82) Alemani, M.; Peters, M. V.; Hecht, S.; Rieder, K.-H.; Moresco, F.; Grill, L. Electric Field-Induced Isomerization of Azobenzene by STM. *J. Am. Chem. Soc.* **2006**, *128* (45), 14446−14447.
(83) Huang, X.; Tang, C.; Li, J.; Chen, L.-C.; Zheng, J.; Zhang, P.; Le, J.; Li, R.; Li, X.; Liu, J.; Yang, Y.; Shi, J.; Chen, Z.; Bai, M.; Zhang, H.-L.; Xia, H.; Cheng, J.; Tian, Z.-Q.; Hong, W. Electric Field-Induced Selective Catalysis of Single-Molecule Reaction. *Sci. Adv.* **2019**, *5* (6), eaaw3072.
(84) Morozov, A. N.; Mebel, A. M.; Frenklach, M. Acceleration of a Chemical Reaction Due to Nonequilibrium Collisional Dynamics: Dimerization of Polyaromatics. *J. Phys. Chem. Lett.* **2022**, *13* (49), 11528−11535.
(85) Veronesi, S.; Commodo, M.; Basta, L.; De Falco, G.; Minutolo, P.; Kateris, N.; Wang, H.; D'Anna, A.; Heun, S. Morphology and Electronic Properties of Incipient Soot by Scanning Tunneling Microscopy and Spectroscopy. *Combust. Flame* **2022**, *243*, 111980.
(86) Commodo, M.; De Falco, G.; Bruno, A.; Borriello, C.; Minutolo, P.; D'Anna, A. Physicochemical Evolution of Nascent Soot Particles in a Laminar Premixed Flame: From Nucleation to Early Growth. *Combust. Flame* **2015**, *162* (10). 3854.
(87) de Falco, G.; Commodo, M.; D'Anna, A.; Minutolo, P. The Evolution of Soot Particles in Premixed and Diffusion Flames by Thermophoretic Particle Densitometry. *Proceedings of the Combustion Institute* **2017**, *36* (1), 763.
(88) Abid, A. D.; Heinz, N.; Tolmachoff, E. D.; Phares, D. J.; Campbell, C. S.; Wang, H. On Evolution of Particle Size Distribution Functions of Incipient Soot in Premixed Ethylene-Oxygen-Argon Flames. *Combust. Flame* **2008**, *154* (4), 775−788.
(89) McEnally, C. S.; Köylü, Ü. Ö.; Pfefferle, L. D.; Rosner, D. E. Soot Volume Fraction and Temperature Measurements in Laminar Nonpremixed Flames Using Thermocouples. *Combust. Flame* **1997**, *109* (4), 701−720.
(90) Rapenne, G.; Grill, L.; Zambelli, T.; Stojkovic, S. M.; Ample, F.; Moresco, F.; Joachim, C. Launching and Landing Single Molecular Wheelbarrows on a Cu(100) Surface. *Chem. Phys. Lett.* **2006**, *431* (1−3), 219−222.
(91) Zhang, Y.; Schuler, B.; Fatayer, S.; Gross, L.; Harper, M. R.; Kushnerick, J. D. Understanding the Effects of Sample Preparation on the Chemical Structures of Petroleum Imaged with Noncontact Atomic Force Microscopy. *Ind. Eng. Chem. Res.* **2018**, *57* (46), 15935−15941.
(92) Schuler, B.; Zhang, Y.; Collazos, S.; Fatayer, S.; Meyer, G.; Pérez, D.; Guitián, E.; Harper, M. R.; Kushnerick, J. D.; Peña, D.; Gross, L. Characterizing Aliphatic Moieties in Hydrocarbons with Atomic Force Microscopy. *Chem. Sci.* **2017**, *8* (3), 2315−2320.
(93) Meyer, G. A Simple Low-temperature Ultrahigh-vacuum Scanning Tunneling Microscope Capable of Atomic Manipulation. *Rev. Sci. Instrum.* **1996**, *67* (8), 2960−2965.
(94) Mohn, F. *Probing Electronic and Structural Properties of Single Molecules on the Atomic Scale*. PhD Thesis, Universität Regensburg, 2012. DOI: 10.5283/epub.25245.
(95) Gross, L.; Schuler, B.; Pavliček, N.; Fatayer, S.; Majzik, Z.; Moll, N.; Peña, D.; Meyer, G. Atomic Force Microscopy for Molecular Structure Elucidation. *Angew. Chem., Int. Ed.* **2018**, *57* (15), 3888−3908.
(96) Giessibl, F. J. High-Speed Force Sensor for Force Microscopy and Profilometry Utilizing a Quartz Tuning Fork. *Appl. Phys. Lett.* **1998**, *73* (26), 3956−3958.
(97) Albrecht, T. R.; Grütter, P.; Horne, D.; Rugar, D. Frequency Modulation Detection Using High-Q Cantilevers for Enhanced Force Microscope Sensitivity. *J. Appl. Phys.* **1991**, *69* (2), 668−673.
(98) Bartels, L.; Meyer, G.; Rieder, K.-H. Controlled Vertical Manipulation of Single CO Molecules with the Scanning Tunneling Microscope: A Route to Chemical Contrast. *Appl. Phys. Lett.* **1997**, *71* (2), 213−215.
(99) Gross, L.; Mohn, F.; Moll, N.; Schuler, B.; Criado, A.; Guitián, E.; Peña, D.; Gourdon, A.; Meyer, G. Bond-Order Discrimination by Atomic Force Microscopy. *Science* **2012**, *337* (6100), 1326−1329.
(100) Hapala, P.; Kichin, G.; Wagner, C.; Tautz, F. S.; Temirov, R.; Jelínek, P. Mechanism of High-Resolution STM/AFM Imaging with Functionalized Tips. *Phys. Rev. B* **2014**, *90* (8), 085421.
(101) Mohn, F.; Schuler, B.; Gross, L.; Meyer, G. Different Tips for High-Resolution Atomic Force Microscopy and Scanning Tunneling Microscopy of Single Molecules. *Appl. Phys. Lett.* **2013**, *102* (7), 073109.
(102) Moll, N.; Gross, L.; Mohn, F.; Curioni, A.; Meyer, G. The Mechanisms Underlying the Enhanced Resolution of Atomic Force Microscopy with Functionalized Tips. *New J. Phys.* **2010**, *12* (12), 125020.
(103) Smith, D. G. A.; Burns, L. A.; Simmonett, A. C.; Parrish, R. M.; Schieber, M. C.; Galvelis, R.; Kraus, P.; Kruse, H.; di Remigio, R.; Alenaizan, A.; James, A. M.; Lehtola, S.; Misiewicz, J. P.; Scheurer, M.; Shaw, R. A.; Schriber, J. B.; Xie, Y.; Glick, Z. L.; Sirianni, D. A.; O'Brien, J. S.; Waldrop, J. M.; Kumar, A.; Hohenstein, E. G.; Pritchard, B. P.; Brooks, B. R.; Schaefer, H. F.; Sokolov, A. Yu.; Patkowski, K.; DePrince, A. E.; Bozkaya, U.; King, R. A.; Evangelista, F. A.; Turney, J. M.; Crawford, T. D.; Sherrill, C. D. Psi4 1.4: Open-Source Software for High-Throughput Quantum Chemistry. *J. Chem. Phys.* **2020**, *152* (18), 184108.
(104) Neese, F. The ORCA Program System. *WIREs Computational Molecular Science* **2012**, *2* (1), 73−78.
(105) Lu, T.; Chen, F. Multiwfn: A Multifunctional Wavefunction Analyzer. *J. Comput. Chem.* **2012**, *33* (5), 580−592.
(106) Humphrey, W.; Dalke, A.; Schulten, K. VMD: Visual Molecular Dynamics. *J. Mol. Graph* **1996**, *14* (1), 33−38.

https://doi.org/10.1021/acsnano.3c02194
ACS Nano 2023, 17, 13563−13574